Classification: Biophysics and Computational Biology

Quantum mechanics/molecular mechanics simulation of the ligand vibrations of the water-oxidizing Mn_4CaO_5 cluster in photosystem II

Shin Nakamura, and Takumi Noguchi*

Division of Material Science, Graduate School of Science, Nagoya University, Furo-cho, Chikusa-ku, Nagoya, 464-8602, Japan

*Corresponding author:

Takumi Noguchi

E-mail: tnoguchi@bio.phys.nagoya-u.ac.jp. Telephone: +81-52-789-2881. Fax: +81-52-789-2883.

Short title: QM/MM simulation of ligand vibrations of the Mn_4CaO_5 cluster

Keywords: photosynthesis; water oxidation; QM/MM; FTIR

Abstract: During photosynthesis, the light-driven oxidation of water performed by photosystem II (PSII) provides electrons necessary to fix CO_2, in turn supporting life on Earth by liberating molecular oxygen. Recent high-resolution X-ray images of PSII show that the water-oxidizing center (WOC) is composed of a Mn_4CaO_5 cluster with six carboxylate, one imidazole, and four water ligands. Fourier transform infrared (FTIR) difference spectroscopy has shown significant structural changes of the WOC during the S-state cycle of water oxidation, especially within carboxylate groups. However, the roles these carboxylate groups play in water oxidation, as well as how they should be properly assigned in spectra, are unresolved. In this study, we performed a normal mode analysis of the WOC using the quantum mechanics/molecular mechanics (QM/MM) method to simulate FTIR difference spectra upon the S_1-to-S_2 transition in the carboxylate stretching region. By evaluating WOC models with different oxidation and protonation states, we determined that models of high-oxidation states, $Mn(III)_2Mn(IV)_2$, satisfactorily reproduced experimental spectra from intact and Ca-depleted PSII when compared to low-oxidation models. It is further suggested that the carboxylate groups bridging Ca and Mn ions within this center tune the reactivity of water ligands bound to Ca by shifting charge via their π conjugation.

Significance Statement

Photosystem II plays an important role in photosynthesis by oxidizing water; this process provides as an electron source to fix CO_2 during photosynthesis, which sustains life on Earth by liberating molecular oxygen. Although the catalytic site, the water-oxidizing center (WOC), is known to consist of a Mn_4CaO_5 cluster and six carboxylate and one imidazole ligands, its detailed structure and reaction mechanism have not yet been resolved. In this study, we successfully simulated the carboxylate stretching region of the experimental infrared spectra of WOC by calculating WOC vibrations using the quantum mechanics/molecular mechanics method. Our simulations demonstrate the significant role that carboxylate groups bridging Mn and Ca play in tuning the water oxidation reaction.

Introduction

The oxidation of water, performed by photosystem II (PSII) in plants and cyanobacteria, is a crucial part of the photosynthesis process, providing a source of electrons used for CO_2 fixation. This process also produces molecular oxygen, as a byproduct; this 'waste' oxygen is released to the atmosphere, where it plays an essential role in sustaining life on Earth. The catalytic site of water oxidation is a water-oxidizing center (WOC) located in the electron-donor side of PSII (1-3). Recent high-resolution (1.9–1.95 Å) X-ray crystallographic structures of PSII (4, 5) revealed that the WOC core is a Mn_4CaO_5 cluster fixed to the protein by six carboxylate [D1-D170, D1-E189, D1-E333, D1-D342, D1-A344 (C-terminus), and CP43-E354] ligands and one imidazole (D1-H332) ligand. Four water ligands are also bound to Mn4 (W1 and W2) and Ca (W3 and W4) (see Fig. 1B for numbering of the Mn ions and water ligands); several water molecules also exist around the Mn_4CaO_5 cluster, forming a hydrogen bond network (Fig. 1A). Because of the absence of the information of hydrogen atoms in the X-ray structures, however, the protonation states of the water and oxo ligands in Mn_4CaO_5 as well as the structure of the hydrogen-bond network remain to be clarified.

The water-oxidizing reaction proceeds through a cycle of five intermediates designated as S_n states (n = 0−4) (6, 7), where S_1 is the most stable in the dark. Oxidation of the Mn_4CaO_5 cluster by a $Y_Z^{\bullet}$ radical, produced by light-induced charge separation, advances the S_n state (n = 0−3) to the S_{n+1} state. The S_4 state immediately relaxes to the S_0 state upon release of O_2. The oxidation states of the Mn atoms within the cluster has long been a source of debate, especially around whether the cluster exists in a high-oxidation [$Mn(III)_2Mn(IV)_2$] or low-oxidation [$Mn(III)_4$ or

$Mn(II)Mn(III)_2Mn(IV)]$ state in S_1 (8-12).

With the information of atomic coordinates from high-resolution X-ray structures of the WOC, quantum chemical calculation is now a very powerful method in investigation of the water oxidation mechanism (10, 12-24). Calculations using the density functional theory (DFT) and quantum mechanics/molecular mechanics (QM/MM) methods can be used to predict individual S-state structures and hence the reaction scheme. Experimental data such as electron paramagnetic resonance (EPR) and extended X-ray absorption fine structure (EXAFS) as well as X-ray structural information were simulated using these methods to identify the protonation structure and the oxidation states (10, 13, 15, 20, 21), although a definite conclusion has not yet been reached.

In contrast to EPR and EXAFS, which provide information mainly about the Mn_4CaO_5 core, Fourier transform infrared (FTIR) spectroscopy provides structural information about the protein moiety and water molecules coupled to the Mn_4CaO_5 cluster (25-27). FTIR spectroscopy, which detects molecular vibrations, is highly sensitive to the structures and interactions of functional groups, and hence the FTIR difference technique can recognize subtle structural changes at a much finer structural resolution than X-ray crystallography. Flash-induced FTIR difference spectra taken during the S-state cycle show many prominent signals in the protein region. In particular, characteristic features were observed around 1400 cm^{-1} in the region of the symmetric stretching vibrations of carboxylate groups (28-35). Such signals reflect significant changes in the interactions of carboxylate groups around the Mn_4CaO_5 cluster, implying that these carboxylate groups are deeply involved in the water

oxidation mechanism. The observation that Ca^{2+} depletion drastically changed the spectral feature around 1400 cm^{-1} (28, 36) also supports this. Thus, analyzing the structural changes of carboxylate groups during the S-state cycle provides crucial information regarding the mechanism of this reaction. However, clear assignment of the FTIR bands to individual carboxylate groups has not been achieved, except for the C-terminal carboxylate of D1-Ala344, whose bands were assigned successfully by its selective labeling with [1-^{13}C]Ala (31, 32).

In this study, the carboxylate stretching region of the FTIR difference spectra of the WOC was simulated using QM/MM calculations, which were based on a damage-free X-ray structure obtained using an X-ray free electron laser (XFEL) (5). Several WOC models with different oxidation and protonation states (Table 1) were assumed to reproduce the experimental S_2/S_1 difference (30) and $^{12}C/^{13}C$-Ala S_2/S_1 double difference (31) spectra. The S_2/S_1 difference spectrum of a Ca-depleted WOC (28) was also simulated. These FTIR spectra show subtle changes in bond lengths and interactions of carboxylate groups, thus providing a different way of evaluating the most accurate WOC model from previous simulations using EXAFS and EPR data (10, 13, 15, 20, 21). The present QM/MM simulation provides sufficient reproduction of the FTIR spectra, demonstrating the significance of carboxylate ligands in the water oxidation mechanism.

Results

The QM region of the WOC used in QM/MM calculations (Fig. 1A) included six carboxylate ligands (D170, E189, E333, D342, E354, and A344; subunit names are

omitted hereafter) and one nearby carboxylate group (D61) hydrogen bonded with W1 (Fig. 1B). All the amino acid groups and water molecules interacting with these carboxylate groups were included in the QM region to accurately reproduce carboxylate vibrations. Different protonation states at W2 and O5, as well as high- and low-oxidation states of the Mn ions, were assumed in the constructed models (Table 1). Model ***1*** (W2/O5 = H_2O/O^{2-}) and model ***2*** (W2/O5 = OH^-/O^{2-}), which both have high oxidation states, have been used in many previous DFT and QM/MM studies (10, 14, 16, 18-20, 22), while model ***3*** (W2/O5 = OH^-/H_2O) and model ***4*** (W2/O5 = H_2O/OH^-) have low-oxidation states that previous DFT calculations suggested could fit to the 1.9 and 1.95 Å structures, respectively, revealed by X-ray crystallography (12). A model of a Ca-depleted WOC with the same protonation and oxidation states as model ***1*** was also calculated (model ***5***: Fig. S2). In the S_2 state, Mn1 or Mn4 was oxidized in the high-oxidation models, while Mn2 or Mn4 was oxidized in the low-oxidation models. The Mn1- and Mn4-oxidized S_2 states of the high-oxidation models have been proposed to reflect two conformations showing g = 4.1 and g = 2 multiline EPR signals, respectively, where the latter conformation has a slightly lower energy (10, 14, 17).

The optimized Mn_4CaO_5 cluster geometries, specifically, metal-metal, metal-O, metal-water (O), and metal-ligand (O or N) distances, together with deviations from the XFEL X-ray structure (5), are summarized in Table S1. Model ***1*** and ***2*** showed relatively small deviations (RMSD = 0.12–0.13 Å), whereas model ***3*** and ***4*** showed larger deviations (RMSD = 0.25 and 0.15 Å). In particular, model ***3*** has a very large deviations in Mn3-O5 and Mn4-O5 (0.93 and 0.86 Å, respectively). The calculated distances of model ***1*** are very similar to those in previous QM/MM calculations (18, 19).

A relatively large deviation of Mn3-O5 (−0.44 Å) from the XFEL structure could be attributed to a minor contribution of the S_0 state as previously suggested (20). Infrared spectra of the WOC were simulated within the symmetric COO^- stretching region at around 1400 cm^{-1}. This region does not overlap with other vibrational modes, in contrast to a severe overlap of the strong amide II bands in the asymmetric COO^- region around 1550 cm^{-1} (29). Simulated S_2/S_1 infrared difference spectra of model ***1*** agreed well with the experimental spectrum (30) for both the S_2 states oxidized at Mn1 and Mn4 (Fig. 2Aa). In particular, the prominent negative band present at 1401 cm^{-1} with positive bands on both the higher- and lower-frequency sides of this peak was well reproduced. The $^{12}C/^{13}C$-Ala S_2/S_1 double difference spectra calculated using model ***1***, with both the Mn1- and Mn4-oxidized S_2 sates, also well reproduced the experimental spectrum obtained by Chu et al. (31), which showed major bands at 1356(−)/1339(+)/1320(+)/1302(−) representing the vibrations of the C-terminal carboxylate of D1-A344 (Fig. 2Ba). The calculated spectra of model ***2***, with the S_2 states oxidized at Mn1 and Mn4, also showed features similar to those of the experimental S_2/S_1 difference spectrum (Fig. 2Ab) and are in good agreement with the $^{12}C/^{13}C$-Ala S_2/S_1 double difference spectrum (Fig. 2Bb). In contrast to high-oxidation models, the low-oxidation models, ***3*** and ***4***, poorly reproduced the S_2/S_1 difference spectrum (Fig. 2Ac, d). The $^{12}C/^{13}C$-Ala S_2/S_1 difference spectrum was also not reproduced by model ***3*** (Fig. 2Bc), although model ***4*** reproduced major features of the $^{12}C/^{13}C$-A344 difference spectrum (Fig. 2Bd).

The calculated normal modes of symmetric COO^- vibrations of model ***1*** in the S_1 and Mn4-oxidized S_2 states are depicted under the simulated S_2/S_1 spectrum in Fig.

3A (normal modes of other high-oxidation models are shown in Fig. S3, and assignments are summarized in Tables S2 and S3). Most of the COO^- vibrations show significant couplings among carboxylate groups, although lower frequency bands at 1350-1250 cm^{-1} arise from isolated vibrations of A344 and E189, which bridge Mn and Ca ions. It is notable that the prominent negative band at 1401 cm^{-1} arises mainly from the isolated vibration of D170 in model ***1*** (Fig. 3A; Fig. S3A). The vibration of E333 also contributes to the lower-frequency side of the band. In the S_2 state, these vibrations are downshifted to ~1360 cm^{-1}. The bands at 1436/1418 cm^{-1} may be assigned to the vibrations of D61, D342, and E189 calculated at 1450-1420/~1410 cm^{-1} (Figs. 3A and S3A); the deviations from the experimental frequencies may be due to slightly different scaling factors depending on the vibrational modes. The same tendency was also found in model ***2*** (Fig. S3B, C). In this case, however, E333 is the main vibration for the 1401 cm^{-1} band, while D170 contributes to the higher-frequency band together with D61 and D342. Thus, deprotonation of W2 induces a slight rearrangement of COO^- vibrations without drastic changes in their frequencies (see SI text for detailed discussion about the effect of W2 deprotonation).

Downshifts in frequencies associated with D170 and E333 are consistent with changes in CO lengths within COO^- (Table 2); the CO bond interacting with Mn4 has a longer length than the other CO bond interacting with Ca (D170) or Mn3 (E333) in the S_1 state, and the former CO further lengthens upon S_2 formation, whereas the latter CO is shortened. This asymmetric structure weakens the coupling of two CO vibrations within the COO^- group. This increases the contribution of the longer CO bond in the 'symmetric' COO^- stretching vibration, resulting in observed frequency downshifts.

The CO length changes in D170 and E333 are induced by stronger interactions with Mn4, as shown in the tendency towards shortened distances of D170-Mn4 and E333-Mn4 (Table S1) upon S_2 formation.

Normal modes in the simulated $^{12}C/^{13}C$-Ala S_2/S_1 double difference spectrum are shown in Fig. 3B for model ***1*** with a Mn4-oxidized S_2 state. It is clear that the major experimental bands at 1356/1339/1320/1302 cm^{-1} arise from ^{13}C-induced shifts of isolated A344 vibrations at 1356(S_1)/1339(S_2) cm^{-1} to 1320(S_1)/1302(S_2) cm^{-1} by 36–37 cm^{-1}. The relatively low frequency of the A344 vibration, and the 17 cm^{-1} downshift upon S_2 formation, are consistent with its asymmetric structure and an increased asymmetry upon S_2 formation; it has longer (1.294 Å) and shorter (1.236 Å) CO bonds on the Mn2 and Ca sides, respectively, which changes by +0.0005 and −0.0001 Å, respectively (Table S1). Weak coordination to Ca is reflected in the distance of A344-Ca (2.54 Å), which is long relative to A344-Mn2 (1.91 Å), in good agreement with experimental values (2.43 and 1.90 Å, respectively; Table S1). This is also consistent with experimental observations that the A344 bands are insensitive to the replacement of Ca^{2+} with Sr^{2+} (32). Similar trends in vibrational frequencies and bond lengths within A344 are also found in other high-oxidation models (Fig. S3, Table 2, and Table S1).

A simulated S_2/S_1 difference spectrum of the Ca-depleted WOC (model ***5***), which is shown in Fig. 4 with band assignments, is in good agreement with the experimental spectrum (28). In particular, the isolated D170 vibration at ~1400 cm^{-1} in the intact WOC (Fig. 3A) is downshifted to ~1350 cm^{-1}, and a positive feature around 1360 cm^{-1} arising from the coupled D170 vibrations is lost. These alterations are

consistent with a change from bidentate to unidentate coordination upon Ca^{2+} removal, which is reflected in variations in CO lengths (specifically, +0.024 and −0.030 Å on the Mn4 and free sides; Table 2). Vibrations of other carboxylate groups are also rearranged significantly upon Ca^{2+} depletion (Fig. 4).

Discussion

A number of theoretical simulations of the Mn_4CaO_5 cluster have been attempted to clarify details regarding its structure and physical properties. Most of these simulations focused on the geometry and the spin properties of the Mn_4CaO_5 cluster to reproduce the X-ray structure, as well as EXAFS and EPR data (10, 13, 15, 20, 21). In a recent study, Chuah et al. (23) performed DFT calculations on the Mn_4CaO_5 cluster with its first-shell ligands to outline how carboxylate stretching frequencies behave upon Mn oxidation and deprotonation. In this study, we present the first successful simulation of the FTIR difference spectra of the WOC in the carboxylate stretching region; to do this, we performed QM/MM calculations with a large QM region including nearby amino acids and water molecules in addition to first-shell ligands (Fig. 1A).

Our calculations satisfactorily reproduced the symmetric COO^- stretching region of the experimental S_2/S_1 difference spectrum (30) by using high-oxidation models (models ***1*** and ***2***), which have an oxidation state of (III, IV, IV, III) in the S_1 state (Fig. 2A a, b). Model ***1*** showed a slightly better reproduction when compared to model ***2***. Both of the high-oxidation models also showed a good reproduction of the $^{12}C/^{13}C$-A344 S_2/S_1 double difference spectrum (31) (Fig. 2Ba,b), which specifically

represents the A344 (C-terminal carboxylate) bands. This indicates that the A344 vibrations in the S_1 and S_2 states are estimated correctly by calculations. In addition, the Ca-depleted model (model ***5***) showed a good agreement with the experimental S_2/S_1 difference spectrum of Ca-depleted PSII (28) (Fig. 4). These successful reproductions of experimental spectra lend credibility to the QM/MM calculations and proposed assignments of prominent spectral features (Figs. 3 and 4).

In contrast to the high-oxidation models, both of the low-oxidation models (models ***3*** and ***4***; Table 1) did not reproduce the S_2/S_1 difference spectrum (Fig. 2Ac, d). In addition, the $^{12}C/^{13}C$-Ala difference spectrum was not reproduced by model ***3***, although the major spectral feature was reproduced by model ***4*** (Fig. 2Bc, d). Thus, low-oxidation models previously used to reproduce X-ray structures (12) are unlikely according to carboxylate vibrations. Previous DFT simulations of EXAFS and EPR data also support this conclusion (10).

The QM region used in vibrational analysis includes the six carboxylate ligands surrounding the Mn_4CaO_5 cluster and the D61 hydrogen bonded to W1. The result that simulations with this QM region reproduced the experimental FTIR difference spectra in the COO^- stretching region indicates that the COO^- bands in the spectra originate mostly from these seven carboxylate groups closely interacting with the Mn_4CaO_5 cluster. The vibrations of these carboxylate groups are coupled significantly with each other in most normal modes (Fig. 3A). Upon formation of S_2, carboxylate groups are rearranged without drastic changes in coordination, resulting in frequency shifts and alteration in couplings shown in the simulated S_2/S_1 difference spectrum (Fig. 3A). Because strong couplings exist among carboxylate groups alongside charge

delocalization (Table S4), we conclude that virtually all of the carboxylate groups contribute to the experimental spectrum (Fig. 3A). Among the normal modes, D170 and E333, ligands bound to Mn4, have rather isolated vibrations at ~1400 cm^{-1} in S_1, which change to coupled vibrations at ~1360 cm^{-1} upon S_2 formation, providing prominent bands at these positions in the difference spectrum (Fig. 3A). In addition, the calculated Mulliken charges (Table S4) show that an additional charge is distributed largely to Mn4 not only when Mn4 is oxidized but also when Mn1 is formally oxidized upon S_2 formation. This increased charge at Mn4 induces frequency downshifts of carboxylate ligands. Thus, this charge distribution to Mn4 explains the major contribution of the Mn4 ligands (D170 and E333) to the spectral feature, and further explains the unexpected similarity between the calculated spectra with Mn1- and Mn4-oxidized S_2 states (Fig. 2Aa). Large changes in Mn4 ligands are consistent with a recent QM/MM analysis of the S_2-minus-S_1 difference Fourier map from XFEL X-ray diffraction data (37), which suggests that the main structural change during the $S_1 \rightarrow S_2$ transition is in the position of Mn4 and its coordination environment (38). Krewald et al. (10) also suggested that the $S_1 \rightarrow S_2$ transition should mostly affect the D170 and E333 vibrations due to Mn4(III)'s loss of Jahn-Teller axis upon oxidation. The experimental observation that the prominent negative band at ~1400 cm^{-1} is lost upon Ca^{2+} depletion (28, 36) is also consistent with the assignment of this band to D170 bridging Mn4 and Ca; the spectral change is well explained in calculation of the Ca-depleted WOC (model **5**), in which the D170 vibration downshifts to ~1350 cm^{-1} due to a change from bidentate to unidentate coordination (Fig. 4). Assigning the ~1400 cm^{-1} band to a carboxylate bridge between Mn and Ca was previously proposed from this FTIR observation (28).

Site-directed mutagenesis of cyanobacteria has been used to investigate how carboxylate amino acid residues are involved in COO^- vibrations of FTIR difference spectra of S-state transitions (33-35, 39-47). In contrast to selective isotope labeling using [1-^{13}C]A344 (31, 32), the effects of mutation on FTIR spectra are not straightforward due to the full or partial inactivation of the WOC upon mutation of critical residues, secondary effects on WOC structure, and rearrangement of vibrational couplings of carboxylate groups. Upon E354Q mutation, the S_2/S_1 FTIR difference spectrum showed intensity changes in the 1440-1300 cm^{-1} region, which spans virtually the entire symmetric COO^- region (33, 34). Because the E354 vibration contributes to coupled modes over the 1390–1360 cm^{-1} range in calculated spectra (Fig. 3A), experimental alterations may be explained by rearrangements in the ligand structure, and changes in vibrational couplings that occur in addition to the loss of E354 vibrations. In addition, D61A mutation induced changes in the 1440–1410 and 1370–1320 cm^{-1} region of the S_2/S_1 spectrum (35), which are consistent with major contributions of D61 to coupled modes present at 1420–1410 and 1370–1360 cm^{-1} (Fig. 3A). We note several puzzling observations; specifically, mutations of D170, E189, E333, and D342 induced no or minor changes in the COO^- region in the FTIR difference spectra during the S-state cycle, which is concomitant with little change in oscillation patterns (39-42). These carboxylate ligands are thought to be crucial in supporting the structure of the Mn_4CaO_5 cluster, where their negative charges should be important in determining the redox potential of S-state intermediates. Thus, it is expected that mutations within these carboxylate groups would significantly affect the WOC structure as well as its reactions. In addition, vibrations of these carboxylate

groups are heavily coupled with those of other carboxylate groups (Fig. 3A). Thus, mutation of one of the carboxylate groups (even if it is not coordinated to the formally oxidized Mn) should alter vibrational features, resulting in perturbation in the FTIR difference spectra. Indeed, mutations in amino acid residues that are located far from the Mn_4CaO_5 cluster but interact with it through a hydrogen bond network, such as D2-K317 (43, 44), D1-N181 (45), D1-E65, D2-E312, D1-R334, D1-Q165 (46, 47), showed clear changes in the COO^- region of the FTIR spectra during the S-state cycle. In most cases, the mutations also lowered the efficiency of the $S_3 \rightarrow S_0$ transition. Although recent DFT studies suggested that deprotonation of water/hydroxide ligands coordinating an oxidized Mn suppresses frequency shifts of carboxylate ligands (23, 48), the $S_1 \rightarrow S_2$ transition is not accompanied by release of protons (49); additionally, it is not possible that several carboxylate ligands are all silent in any Mn_4CaO_5 models. Rather, the data in these DFT studies, which showed frequency shifts, to a more or less extent, in virtually all the carboxylate ligands (23, 48), are consistent with our results. Further studies on carboxylate ligands mutants are necessary to resolve discrepancies between the mutational effects on FTIR data and QM/MM calculation results.

We also note a clear trend where D170, A344, and E189, which bridge Mn and Ca, show asymmetric structural changes; this includes lengthened CO bonds on the Mn side and shortened CO bonds on the Ca side upon S_2 formation (Table 2), which results in relatively large frequency downshifts (Fig. 3A). This change is caused by an increase in positive charge on Mn ions upon S_2 formation, which attracts a negative charge on the COO^- group and induces single- and double-bond characters in the CO bonds on Mn and Ca sides, respectively ($Mn...O^-{-}C{=}O...Ca$). This shift of negative charge

through the conjugated COO^- group from the Ca side to the Mn side eventually increases the positive charge on Ca^{2+} (Table S4), which then increases the acidity of water molecules on Ca (W3 and W4). This alteration in charge on Ca is also reflected in a decrease in Ca-W3 and Ca-W4 distances (Table S1), and an increase in OH lengths in W3 and W4 upon S_2 formation (Table S5). It is known that replacing Ca^{2+} with Sr^{2+} decreases the water oxidation rate (50), which can be caused by the difference in Lewis acidity between Ca^{2+} and Sr^{2+} (51, 52). It is thus possible that the W3 and W4 attached to Ca^{2+} are involved in proton release in water oxidation, especially during the $S_2 \rightarrow S_3$ transition, which is inhibited by Ca^{2+} depletion (53). It has also been proposed that W3 moves to Mn4 during the $S_2 \rightarrow S_3$ transition in the so-called oxo-oxyl mechanism (13, 17, 22). Thus, the carboxylate ligands bridging Mn and Ca ions may play an important role in water oxidation by tuning the reactivity of water ligands on Ca by charge shifts via their π conjugation.

Methods

The initial coordinates of PSII models were obtained from the XFEL X-ray structure at a resolution 1.95 Å (5) (PDB ID: 4UB6). In addition to the Mn_4CaO_5 cluster, amino acid residues, water molecules, and two Cl^- ions located within 20 Å from the Mn_4CaO_5 cluster were extracted from the X-ray structure. Hydrogen atoms were generated and optimized using the AMBER force field (54). During this procedure, the positions of all heavy atoms were fixed. QM/MM calculations were performed using the two layer ONIOM method (55) with the electronic embedding scheme within the Gaussian 09 program package (56). The QM region (Fig. 1) consists of the Mn_4CaO_5

cluster, amino acid ligands (D1-D170, D1-E189, D1-E333, D1-D342, D1-A344, and CP43-E354, D1-H332), water ligands (W1, W2, W3, and W4), eleven other water molecules that surround the Mn_4CaO_5 cluster, Y_Z, D1-H190, D1-D61, D1-H337, and CP43-R357. Other atoms in the selected region were assigned to the MM region (Fig. S1). Geometry optimization and normal mode analysis of the QM region were performed using an unrestricted DFT method with the B3LYP functional using LANL2DZ and 6-31G(d) as basis sets for metal atoms and other atoms, respectively (24). In QM/MM geometry optimization, the coordinates of the QM region were fully relaxed, while those of the MM region were fixed. Table 1 shows the oxidation and protonation states of calculated models. The oxidation states of (Mn1, Mn2, Mn3, Mn4) in the S_1 state are (III, IV, IV, III) in high oxidation models and (III, III, III, III) or (III, IV, III, II) in low oxidation models. Mn1 or Mn4 and Mn2 or Mn4 were oxidized upon S_2 formation in the high- and low-oxidation models, respectively. High spin states were assumed in calculations. The protonation states of W2 and O5 were assumed to be H_2O, OH^-, or O^{2-} following previous studies (10, 12-24).

To obtain infrared spectra in the COO^- stretching region, normal modes involving carboxylate vibrations were added by assuming a Gaussian band with a 16 cm^{-1} width (FWHM) for each mode. A scaling factor was determined for each simulated difference spectrum (for models ***1*** and ***2***, an average spectrum of Mn1- and Mn4-oxidized S_2) to adjust the frequency of the simulated major peak to that of the experimental one; this includes the negative peak at 1401 cm^{-1} in the S_2/S_1 difference spectrum, the positive peak at 1320 cm^{-1} in the $^{12}C/^{13}C$-Ala S_2/S_1 double difference spectrum, and the positive peak at 1431 cm^{-1} in the S_2/S_1 difference spectrum of

Ca-depleted PSII. Adopted scaling factors ranged from 0.955 to 0.966. When the corresponding peak was not found in a calculated spectrum, a scaling factor of 0.960 was adopted.

Acknowledgement

We thank Professor Richard J. Debus for providing the data of $^{12}C/^{13}C$-Ala FTIR difference spectrum. QM/MM calculations were performed using Research Center for Computational Science, Okazaki, Japan, and Information Technology Center, Nagoya University. This study was supported by the Grants-in-Aids for JSPS Fellows (15J10320 to S.N.) and for Scientific Research from JSPS (24000018, 24107003, and 25291033 to T.N.).

References

1. McEvoy JP, Brudvig GW (2006) Water-splitting chemistry of photosystem II. *Chem Rev* 106(11):4455–4483.
2. Cox N, Messinger J (2013) Reflections on substrate water and dioxygen formation. *Biochim Biophys Acta* 1827(8-9):1020–1030.
3. Yano J, Yachandra V (2014) Mn_4Ca cluster in photosynthesis: Where and how water is oxidized to dioxygen. *Chem Rev* 114(8):4175–4205.
4. Umena Y, Kawakami K, Shen J-R, Kamiya N (2011) Crystal structure of oxygen-evolving photosystem II at a resolution of 1.9 Å. *Nature* 473(7345):55–60.
5. Suga M, et al. (2015) Native structure of photosystem II at 1.95 Å resolution viewed by femtosecond X-ray pulses. *Nature* 517(7532):99–103.
6. Joliot P, Barbieri G, Chabaud R (1969) Model of the System II photochemical centers.

Photochem Photobiol 10(5):309–329.

7. Kok B, Forbush B, McGloin M (1970) Cooperation of charges in photosynthetic O_2 evolution-I. A linear four step mechanism. *Photochem Photobiol* 11(6):457–475.
8. Roelofs TA, et al. (1996) Oxidation states of the manganese cluster during the flash-induced S-state cycle of the photosynthetic oxygen-evolving complex. *Proc Natl Acad Sci USA* 93(8):3335–3340.
9. Kulik LV, Epel B, Lubitz W, Messinger J (2007) Electronic structure of the Mn_4O_xCa cluster in the S_0 and S_2 states of the oxygen-evolving complex of photosystem II based on pulse ^{55}Mn-ENDOR and EPR spectroscopy. *J Am Chem Soc* 129(44):13421–13435.
10. Krewald V, et al. (2015) Metal oxidation states in biological water splitting. *Chem Sci* 6(3):1676–1695.
11. Zheng M, Dismukes GC (1996) Orbital configuration of the valence electrons, ligand field symmetry, and manganese oxidation states of the photosynthetic water oxidizing complex: Analysis of the S_2 state multiline EPR signals. *Inorg Chem* 35(11):3307–3319.
12. Petrie S, Pace RJ, Stranger R (2015) Resolving the differences between the 1.9 Å and 1.95 Å crystal structures of photosystem II: A single proton relocation defines two tautomeric forms of the water-oxidizing complex. *Angew Chem Int Ed* 54(24):7120–7124.
13. Ames W, et al. (2011) Theoretical evaluation of structural models of the S_2 state in the oxygen evolving complex of photosystem II: Protonation states and magnetic interactions. *J Am Chem Soc* 133(49):19743–19757.
14. Pantazis DA, Ames W, Cox N, Lubitz W, Neese F (2012) Two interconvertible

structures that explain the spectroscopic properties of the oxygen-evolving complex of photosystem II in the S_2 state. *Angew Chem Int Ed* 51(39):9935–9940.

15. Galstyan A, Robertazzi A, Knapp EW (2012) Oxygen-evolving Mn cluster in photosystem II: The protonation pattern and oxidation state in the high-resolution crystal structure. *J Am Chem Soc* 134(17):7442–7449.

16. Siegbahn PEM (2013) Water oxidation mechanism in photosystem II, including oxidations, proton release pathways, O-O bond formation and O_2 release. *Biochim Biophys Acta* 1827(8-9):1003−1019.

17. Bovi D, Narzi D, Guidoni L (2013) The S_2 state of the oxygen-evolving complex of photosystem II explored by QM/MM dynamics: Spin surfaces and metastable states suggest a reaction path towards the S_3 state. *Angew Chem Int Ed* 52(45):11744−11749.

18. Pal R, et al. (2013) S_0-state model of the oxygen-evolving complex of photosystem II. *Biochemistry* 52(44):7703–7706.

19. Saito K, Ishikita H (2014) Influence of the Ca^{2+} ion on the Mn_4Ca conformation and the H-bond network arrangement in Photosystem II. *Biochim. Biophys. Acta* 1837(1):159–166.

20. Askerka M, Vinyard DJ, Wang JM, Brudvig GW, Batista VS (2015) Analysis of the radiation-damage-free X-ray structure of photosystem II in light of EXAFS and QM/MM data. *Biochemistry* 54(9):1713–1716.

21. Li XC, Siegbahn PEM, Ryde U (2015) Simulation of the isotropic EXAFS spectra for the S_2 and S_3 structures of the oxygen evolving complex in photosystem II. *Proc Natl Acad Sci USA* 112(13):3979–3984.

22. Shoji M, Isobe H, Yamaguchi K (2015) QM/MM study of the S_2 to S_3 transition

reaction in the oxygen-evolving complex of photosystem II. *Chem Phys Lett* 636:172–179.

23. Chuah WY, Stranger R, Pace RJ, Krausz E, Frankcombe TJ (2016) Deprotonation of water/hydroxo ligands in clusters mimicking the water oxidizing complex of PSII and its effect on the vibrational frequencies of ligated carboxylate groups. *J Phys Chem B* 120(3):377–385.

24. Nakamura S, Ota K, Shibuya Y, Noguchi T (2016) Role of a water network around the Mn_4CaO_5 cluster in photosynthetic water oxidation: A Fourier transform infrared spectroscopy and quantum mechanics/molecular mechanics calculation study. *Biochemistry* 55(3):597–607.

25. Chu H-A (2013) Fourier transform infrared difference spectroscopy for studying the molecular mechanism of photosynthetic water oxidation. *Front Plant Sci* 4:146.

26. Debus RJ (2015) FTIR studies of metal ligands, networks of hydrogen bonds, and water molecules near the active site Mn_4CaO_5 cluster in Photosystem II. *Biochim Biophys Acta* 1847(1):19–34.

27. Noguchi T (2015) Fourier transform infrared difference and time-resolved infrared detection of the electron and proton transfer dynamics in photosynthetic water oxidation. *Biochim Biophys Acta* 1847(1):35–45.

28. Noguchi T, Ono T, Inoue Y (1995) Direct detection of a carboxylate bridge between Mn and Ca^{2+} in the photosynthetic oxygen-evolving center by means of Fourier transform infrared spectroscopy. *Biochim Biophys Acta* 1228(2-3):189–200.

29. Noguchi T, Sugiura M (2003) Analysis of flash-induced FTIR difference spectra of the S-state cycle in the photosynthetic water-oxidizing complex by uniform ^{15}N and ^{13}C isotope labeling. *Biochemistry* 42(20):6035–6042.

30. Noguchi T, Sugiura M (2002) Flash-induced FTIR difference spectra of the water oxidizing complex in moderately hydrated photosystem II core films: Effect of hydration extent on S-state transitions. *Biochemistry* 41(7):2322–2330.

31. Chu H-A, Hillier W, Debus RJ (2004) Evidence that the C-terminus of the D1 polypeptide of photosystem II is ligated to the manganese ion that undergoes oxidation during the S_1 to S_2 transition: An isotope-edited FTIR study. *Biochemistry* 43(11):3152–3166.

32. Strickler MA, Walker LM, Hillier W, Debus RJ (2005) Evidence from biosynthetically incorporated strontium and FTIR difference spectroscopy that the C-terminus of the D1 polypeptide of photosystem II does not ligate calcium. *Biochemistry* 44(24):8571–8577.

33. Shimada Y, et al. (2009) Effect of a single amino acid substitution of the 43 kDa chlorophyll-protein on the oxygen-evolving reaction of the cyanobacterium *Synechocystis* sp. PCC 6803: Analysis of the Glu354Gln mutation. *Biochemistry* 48(26):6095–6103.

34. Service RJ, et al. (2011) Participation of glutamate-354 of the CP43 polypeptide in the ligation of manganese and the binding of substrate water in photosystem II. *Biochemistry* 50(1):63–81.

35. Debus RJ (2014) Evidence from FTIR difference spectroscopy that D1-Asp61 influences the water reactions of the oxygen-evolving Mn_4CaO_5 cluster of photosystem II. *Biochemistry* 53(18):2941–2955.

36. Taguchi Y, Noguchi T (2007) Drastic changes in the ligand structure of the oxygen-evolving Mn cluster upon Ca^{2+} depletion as revealed by FTIR difference spectroscopy. *Biochim Biophys Acta* 1767(6):535–540.

37. Kern J, et al. (2013) Simultaneous femtosecond X-ray spectroscopy and diffraction of photosystem II at room temperature. *Science* 340(6131):491–495.

38. Askerka M, Wang JM, Brudvig GW, Batista VS (2014) Structural changes in the oxygen-evolving complex of photosystem II induced by the S_1 to S_2 transition: A combined XRD and QM/MM study. *Biochemistry* 53(44):6860–6862.

39. Debus RJ, Strickler MA, Walker LM, Hillier W (2005) No evidence from FTIR difference spectroscopy that aspartate-170 of the D1 polypeptide ligates a manganese ion that undergoes oxidation during the S_0 to S_1, S_1 to S_2, or S_2 to S_3 transitions in photosystem II. *Biochemistry* 44(5)1367–1374.

40. Strickler MA, Hillier W, Debus RJ (2006) No evidence from FTIR difference spectroscopy that glutamate-189 of the D1 polypeptide ligates a Mn ion that undergoes oxidation during the S_0 to S_1, S_1 to S_2, or S_2 to S_3 transitions in photosystem II. *Biochemistry* 45(29):8801–8811.

41. Strickler MA, Walker LM, Hillier W, Britt RD, Debus RJ (2007) No evidence from FTIR difference spectroscopy that aspartate-342 of the D1 polypeptide ligates a Mn ion that undergoes oxidation during the S_0 to S_1, S_1 to S_2, or S_2 to S_3 transitions in photosystem II. *Biochemistry* 46(11):3151–3160.

42. Service RJ, et al. (2013) Participation of glutamate-333 of the D1 polypeptide in the ligation of the Mn_4CaO_5 cluster in photosystem II. *Biochemistry* 52(47):8452–8464.

43. Pokhrel R, Service RJ, Debus RJ, Brudvig GW (2013) Mutation of lysine 317 in the D2 subunit of photosystem II alters chloride binding and proton transport. *Biochemistry* 52(28):4758–4773.

44. Suzuki H, et al. (2013) Functional roles of D2-Lys317 and the interacting chloride ion in the water oxidation reaction of photosystem II as revealed by Fourier transform

infrared analysis. *Biochemistry* 52(28):4748–4757.

45. Pokhrel R, Debus RJ, Brudvig GW (2015) Probing the effect of mutations of asparagine 181 in the D1 subunit of photosystem II. *Biochemistry* 54(8):1663–1672.

46. Service RJ, Hillier W, Debus RJ (2010) Evidence from FTIR difference spectroscopy of an extensive network of hydrogen bonds near the oxygen-evolving Mn_4Ca cluster of photosystem II involving D1-Glu65, D2-Glu312, and D1-Glu329. *Biochemistry* 49(31):6655–6669.

47. Service RJ, Hillier W, Debus RJ (2014), Network of hydrogen bonds near the oxygen-evolving Mn_4CaO_5 cluster of photosystem II probed with FTIR difference spectroscopy. *Biochemistry* 53(6):1001–1017.

48. Terrett R, Frankcombe T, Pace R, Stranger R (2016) Effect of concomitant oxidation and deprotonation of hydrated Mn centres in rationalising the FTIR difference silence of D1-Asp170 in Photosystem II. *J Inorg Biochem* 155:101–104.

49. Suzuki H, Sugiura M, Noguchi T (2009) Monitoring proton release during photosynthetic water oxidation in photosystem II by means of isotope-edited infrared spectroscopy. *J Am Chem Soc* 131(22):7849–7857.

50. Boussac A, Rutherford AW (1988) Nature of the inhibition of the oxygen-evolving enzyme of photosystem II induced by sodium chloride washing and reversed by the addition of Ca^{2+} or Sr^{2+}. *Biochemistry* 27(9):3476–3483.

51. Vrettos JS, Stone DA, Brudvig GW (2001) Quantifying the ion selectivity of the Ca^{2+} site in photosystem II: Evidence for direct involvement of Ca^{2+} in O_2 formation. *Biochemistry* 40(26):7937–7945.

52. Pitari F, Bovi D, Narzi D, Guidoni L (2015) Characterization of the Sr^{2+}- and Cd^{2+}-substituted oxygen-evolving complex of photosystem II by quantum

mechanics/molecular mechanics calculations. *Biochemistry* 54(38):5959–5968.

53. Yocum CF (1991) Calcium activation of photosynthetic water oxidation. *Biochim Biophys Acta* 1059(1):1–15.

54. Case D, et al. (2012) AMBER 12. University of California, San Francisco.

55. Vreven T, et al. (2006) Combining quantum mechanics methods with molecular mechanics methods in ONIOM. *J. Chem. Theory Comput.* 2(3):815–826.

56. Frisch MJ, et al. (2009) Gaussian 09, Revision C.01, Gaussian, Inc., Wallingford CT.

Table 1. Mn_4CaO_5 cluster models used for QM/MM calculations

model	oxidation states in S_1[a]	W2	O5	oxidized Mn in S_2
1	high (III, IV, IV, III)	H_2O	O^{2-}	Mn1 or Mn4
2	high (III, IV, IV, III)	OH^-	O^{2-}	Mn1 or Mn4
3	low (III, III, III, III)	OH^-	H_2O	Mn2
4	low (III, IV, III, II)	H_2O	OH^-	Mn4
5 (Ca dep.)	high (III, IV, IV, III)	H_2O	O^{2-}	Mn4

[a] Oxidation states of (Mn1, Mn2, Mn3, Mn4).

Table 2. CO bond lengths (Å) of carboxylate groups calculated for high-oxidation models

carboxylate[a]	model ***1***			model ***2***			model ***5*** (Ca dep.)	
	length (Å)	ΔS_2 (Mn1)[b]	ΔS_2 (Mn4)[b]	length (Å)	ΔS_2 (Mn1)[b]	ΔS_2 (Mn4)[b]	length (Å)	ΔS_2 (Mn4)[b]
D170(Mn4)	1.271	+0.012	+0.015	1.257	+0.009	+0.019	1.294	+0.025
D170(Ca)	1.265	−0.005	−0.008	1.280	−0.004	−0.013	1.235	−0.009
E189(Mn1)	1.295	+0.009	+0.006	1.297	+0.006	+0.005	1.295	+0.008
E189(Ca)	1.248	−0.003	−0.001	1.244	0.000	0.000	1.236	−0.003
E333(Mn3)	1.266	−0.003	−0.008	1.272	0.000	−0.012	1.262	−0.007
E333(Mn4)	1.277	+0.012	+0.014	1.266	+0.008	+0.017	1.276	+0.013
D342(Mn1)	1.261	+0.014	+0.007	1.260	+0.012	+0.004	1.259	+0.002
D342(Mn2)	1.272	−0.004	−0.002	1.271	−0.004	−0.002	1.269	−0.001
E354(Mn2)	1.287	+0.001	−0.010	1.289	+0.001	−0.008	1.279	−0.008
E354(Mn3)	1.263	+0.006	+0.013	1.258	+0.005	+0.010	1.264	+0.011
A344(Mn2)	1.294	+0.009	+0.005	1.292	+0.009	+0.005	1.304	+0.004
A344(Ca)	1.236	−0.003	−0.001	1.235	−0.004	−0.001	1.225	−0.001
D61(W1)	1.268	+0.011	+0.007	1.263	+0.009	+0.009	1.260	+0.008
D61(W9)	1.262	−0.005	+0.002	1.264	−0.004	−0.006	1.265	−0.004

[a] Interacting metal or water is in parentheses. [b] Change in length by formation of the S_2 state. Oxidized Mn is indicated in parentheses.

Figure Legends

Fig. 1. (A) Optimized structure of the whole QM region in the QM/MM calculation of WOC (model ***1***, S_1 state). Purple, Mn; yellow, Ca; red, O; blue, N; gray, C; cyan, H. E354 and R357 are on the CP43 protein and other residues are on the D1 protein. (B) Carboxylate groups and water ligands around the Mn_4CaO_5 cluster with numbering of Mn and oxygen atoms.

Fig. 2. Calculated infrared spectra in the symmetric COO^- stretching vibrations of carboxylate groups (red or blue lines) in comparison with experimental FTIR difference spectra (black lines). (A) S_2/S_1 difference spectra; (B) $^{12}C/^{13}C$-A344 S_2/S_1 double difference spectra. (a) model ***1*** (blue line, Mn1-oxidized S_2; red line, Mn4-oxidized S_2); (b) model ***2*** (blue line, Mn1-oxidized S_2; red line, Mn4-oxidized S_2); (c) model ***3***; (d) model ***4***. Experimental spectra in (A) and (B) were taken from ref. (30) and ref. (31), respectively.

Fig. 3. Assignments of the symmetric COO^- stretching vibrations of model ***1*** in the S_1 and Mn4-oxidized S_2 states. (A) S_2/S_1 difference spectrum; (B) $^{12}C/^{13}C$-A344 S_2/S_1 double difference spectrum. Calculated normal modes of unlabeled WOC are expressed in black (S_1) and gray (S_2) bars, while those of [1-^{13}C]Ala-WOC are expressed in blue (S_1) and cyan (S_2) bars. Calculated and experimental (30, 31) spectra are shown in red and black lines, respectively. In (B), [1-^{13}C]Ala-induced shifts of calculated major A344 modes are indicated by green dotted arrows.

Fig. 4. A calculated S_2/S_1 infrared difference spectrum in the symmetric COO^- stretching region of the Ca-depleted WOC model (model ***5***; red line) in comparison with the experimental FTIR difference spectrum of Ca-depleted PSII (black line). Calculated normal modes are expressed in black (S_1) and gray (S_2) bars. The experimental spectrum was taken from ref. (28).

Fig. 1

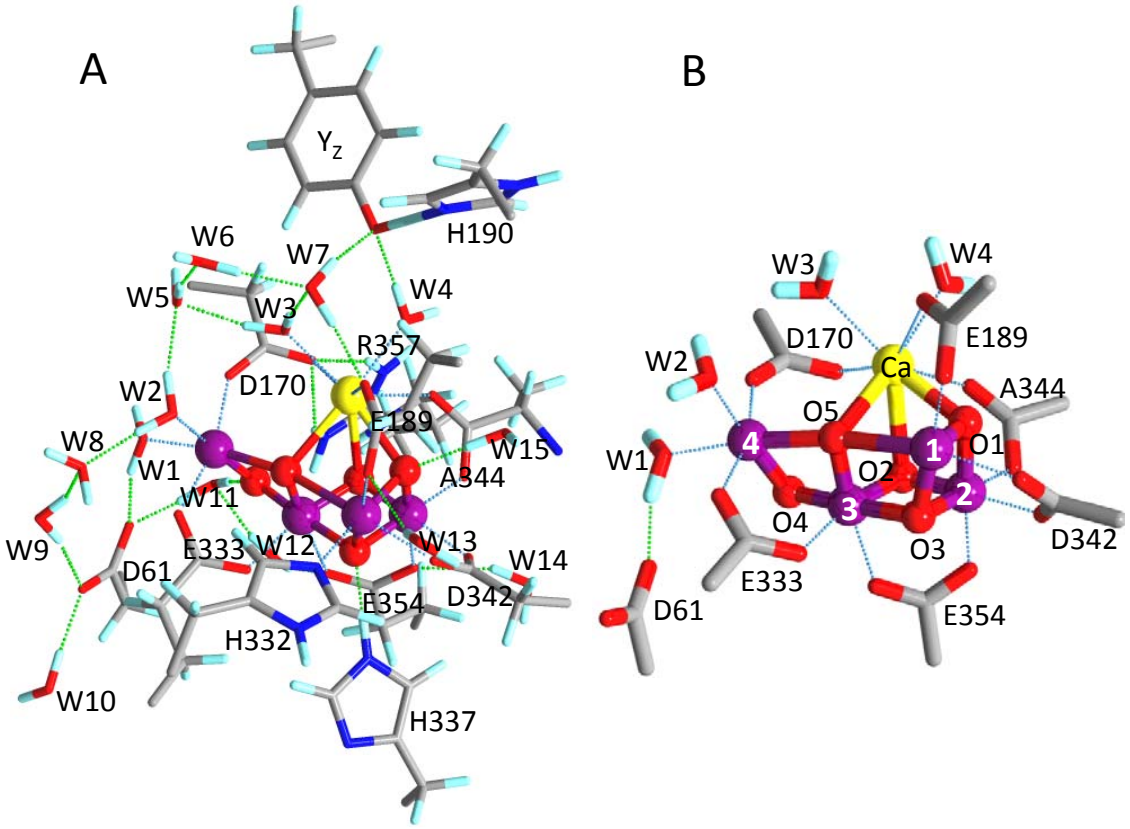
A
B
Y_Z
H190
W6
W7
W4
W5
W3
R357
D170
W2
E189
W8
W15
W1
A344
W11
W9
E333
W12
W13
W14
D61
E354
D342
H332
W10
H337
W3
W4
D170
E189
W2
Ca
A344
O5
4
1
O1
W1
O2
2
3
O4
O3
D342
E333
D61
E354

Fig. 2

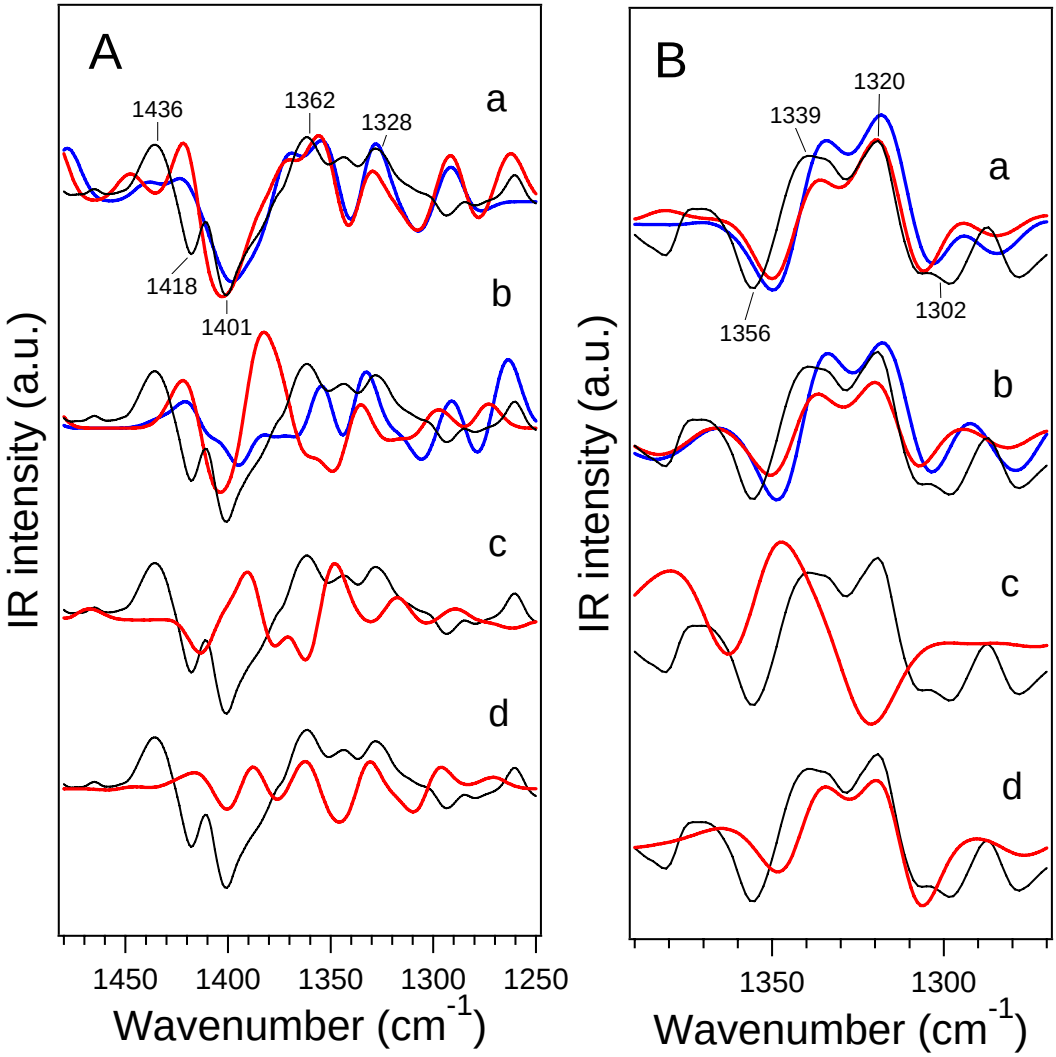
A
1436
1362
1328
a
1418
1401
b
c
d
IR intensity (a.u.)
1450
1400
1350
1300
1250
Wavenumber (cm-1)
B
1320
1339
a
1356
1302
b
c
d
IR intensity (a.u.)
1350
1300
Wavenumber (cm-1)

Fig. 3

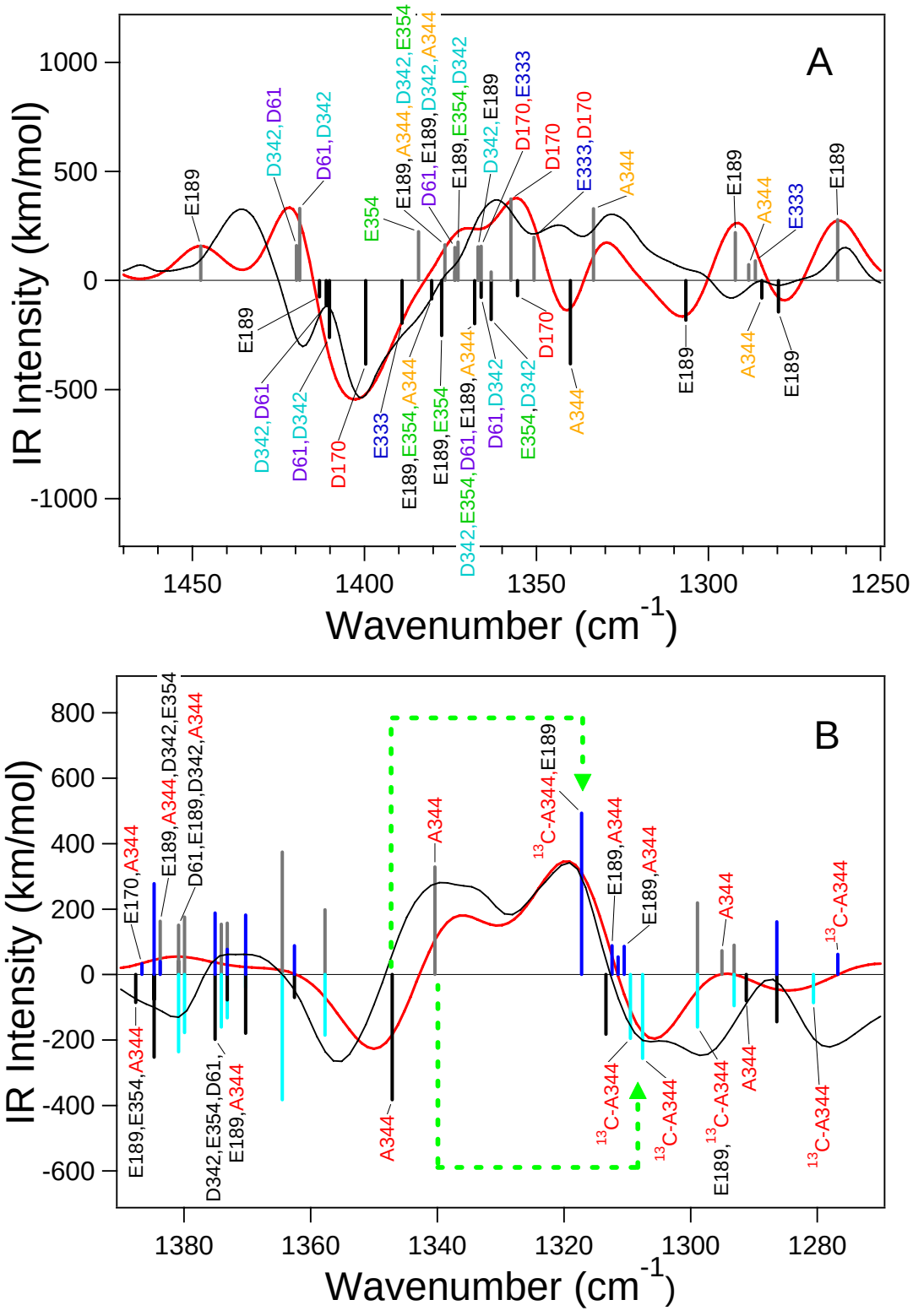
A
IR Intensity (km/mol)
1000
500
0
-500
-1000
1450
1400
1350
1300
1250
Wavenumber (cm-1)
E189
D342,D61
D61,D342
E354
E189,A344,D342,E354
D61,E189,D342,A344
E189,E354,D342
D342,E189
D170,E333
D170
E333,D170
A344
E189
A344
E333
E189
D342,D61
D61,D342
D170
E333
E189,E354,A344
E189,E354
D342,E354,D61,E189,A344
D61,D342
E354,D342
D170
A344
E189
A344
E189
B
IR Intensity (km/mol)
800
600
400
200
0
-200
-400
-600
1380
1360
1340
1320
1300
1280
Wavenumber (cm-1)
E170,A344
E189,A344,D342,E354
D61,E189,D342,A344
A344
13C-A344,E189
E189,A344
E189,A344
A344
13C-A344
E189,E354,A344
D342,E354,D61,
E189,A344
A344
13C-A344
13C-A344
E189,13C-A344
A344
13C-A344

Fig. 4

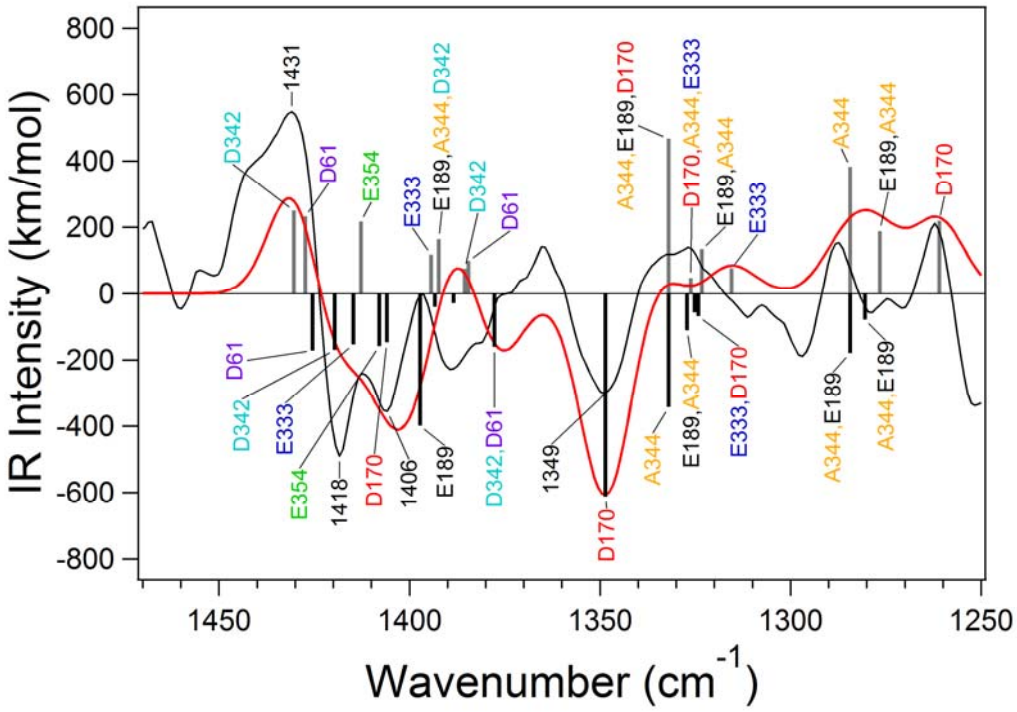
IR Intensity (km/mol)
800
600
400
200
0
-200
-400
-600
-800
1450
1400
1350
1300
1250
Wavenumber (cm-1)
1431
D342
D61
E354
E333
E189,A344,D342
D342
D61
A344,E189,D170
D170,A344,E333
E189,A344
E333
A344
E189,A344
D170
D61
D342
E333
E354
1418
D170
1406
E189
D342,D61
1349
D170
A344
E189,A344
E333,D170
A344,E189
A344,E189

Supporting Information

Quantum mechanics/molecular mechanics simulation of the ligand vibrations of the water-oxidizing Mn_4CaO_5 cluster in photosystem II

Shin Nakamura, and Takumi Noguchi*

Division of Material Science, Graduate School of Science, Nagoya University, Furo-cho, Chikusa-ku, Nagoya, 464-8602, Japan

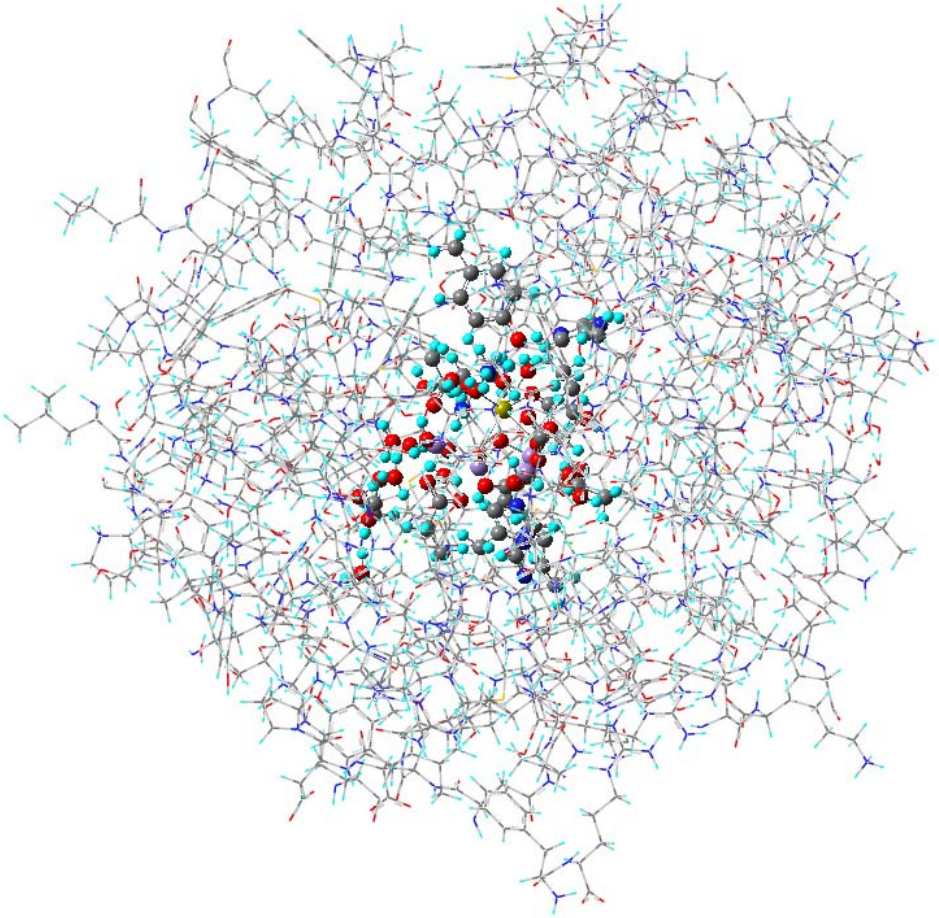

Fig. S1. The whole QM/MM region used for calculation. The MM and QM regions are expressed in wire and ball & stick styles, respectively. Atoms of amino acid residues, water molecules, the Mn_4CaO_5 cluster, and Cl^- ions within 20 Å from the Mn_4CaO_5 were taken from the XFEL X-ray structure of PSII (4UB6) (5), and hydrogen atoms were generated and optimized using Amber.

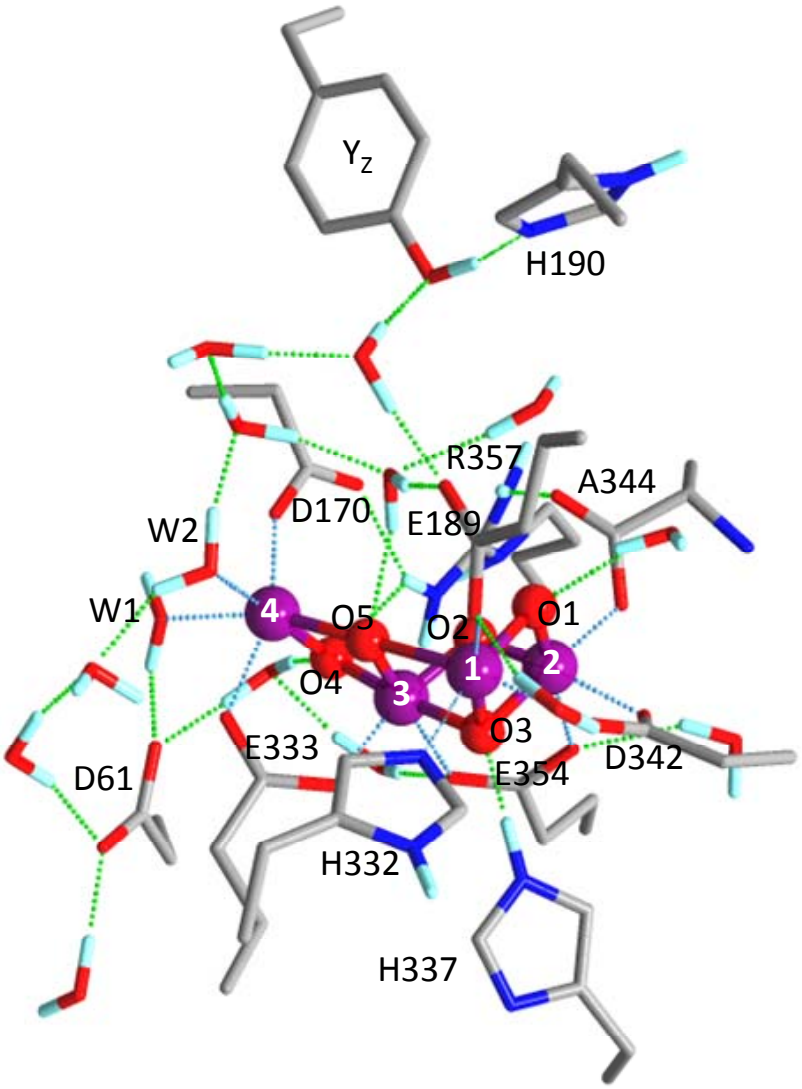

Fig. S2. Optimized structure of the QM region of Ca-depleted WOC (model ***5***). Purple, Mn; red, O; blue, N; gray, C; cyan, H. E354 and R357 are on the CP43 protein and other residues are on the D1 protein. Hydrogen atoms in the hydrocarbon parts of amino acid side chains are omitted.

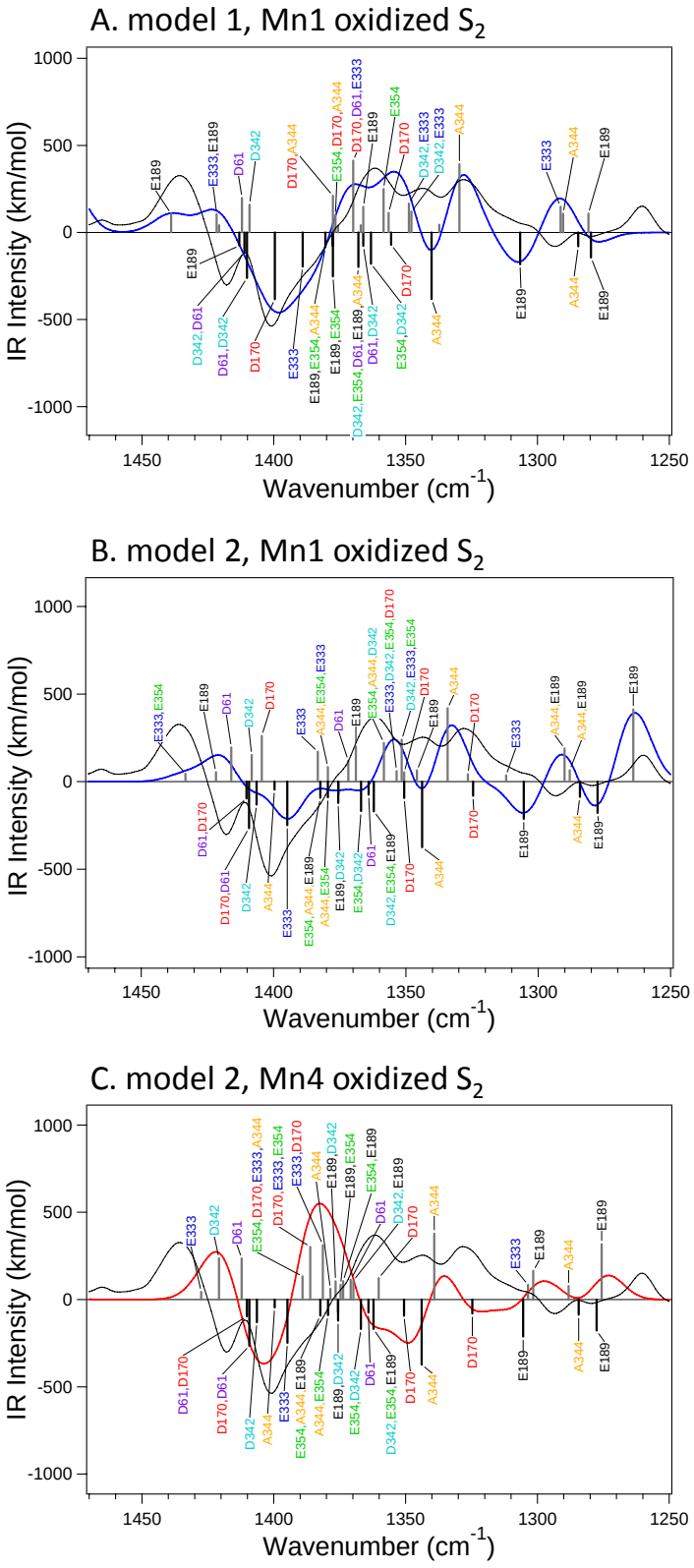

Fig. S3. Assignments of the symmetric COO^- stretching vibrations in the calculated S_2/S_1 difference spectra of models ***1*** (A: Mn1-oxidized S_2) and model ***2***. (B: Mn1-oxidized S_2; C: Mn4-oxidized S_2). Calculated normal modes are expressed in black (S_1) and gray (S_2) bars. Spectra calculated from the normal modes of carboxylate vibrations are shown in blue (Mn1-oxidized S_2) and red (Mn4-oxidized S_2) lines, while the experimental spectrum (30) is expressed by a black line.

Table S1. Atomic distances (Å) of the Mn_4CaO_5 cluster in geometry optimized models

	model ***1***				model ***2***				model ***3***			model ***4***			model ***5*** (Ca dep.)			exp.[d]
	d[a]	Δexp[b]	ΔS_2 (Mn1)[c]	ΔS_2 (Mn4)[c]	*d*[a]	Δexp[b]	ΔS_2 (Mn1)[c]	ΔS_2 (Mn4)[c]	*d*[a]	Δexp[b]	ΔS_2 (Mn2)[c]	*d*[a]	Δexp[b]	ΔS_2 (Mn4)[c]	*d*[a]	Δexp[b]	ΔS_2 (Mn4)[c]	
Mn1-Mn2	2.74	+0.06	−0.01	+0.02	2.74	+0.06	−0.03	0.00	2.79	+0.11	−0.05	2.73	+0.05	0.00	2.72	+0.04	0.00	2.68
Mn1-Mn3	3.17	−0.03	−0.28	+0.18	3.14	−0.06	−0.23	+0.24	3.42	+0.22	0.00	3.23	+0.03	+0.07	3.08	−0.12	+0.24	3.20
Mn1-Mn4	4.86	−0.09	+0.11	+0.05	4.78	−0.17	+0.17	+0.14	5.30	+0.35	−0.03	4.97	+0.02	−0.04	4.57	−0.38	+0.25	4.95
Mn2-Mn3	2.75	+0.05	−0.02	−0.01	2.78	+0.08	−0.02	−0.01	2.78	+0.08	+0.01	2.81	+0.11	−0.03	2.74	+0.04	0.00	2.70
Mn2-Mn4	5.23	+0.02	+0.30	−0.11	5.26	+0.05	+0.30	−0.11	5.47	+0.26	0.00	5.42	+0.21	−0.17	5.06	−0.15	−0.02	5.21
Mn3-Mn4	2.81	−0.06	+0.30	−0.07	2.84	−0.03	+0.28	−0.09	3.10	+0.23	+0.02	3.03	+0.16	−0.11	2.76	−0.11	−0.04	2.87
Mn1-Ca	3.45	−0.02	−0.07	+0.12	3.44	−0.03	−0.05	+0.13	3.57	+0.10	+0.07	3.40	−0.07	+0.11	–	–	–	3.47
Mn2-Ca	3.45	+0.13	+0.09	+0.04	3.46	+0.14	+0.08	+0.02	3.42	+0.10	+0.02	3.44	+0.12	+0.03	–	–	–	3.32
Mn3-Ca	3.49	+0.09	+0.06	+0.16	3.49	+0.09	+0.05	+0.13	3.75	+0.35	+0.06	3.62	+0.22	+0.07	–	–	–	3.40
Mn4-Ca	3.85	+0.08	+0.27	+0.07	3.82	+0.05	+0.26	+0.06	4.23	+0.46	+0.01	3.96	+0.19	−0.09	–	–	–	3.77
Mn1-O1	1.86	+0.06	−0.02	+0.01	1.86	+0.06	−0.03	0.00	1.78	−0.02	+0.09	1.87	+0.07	−0.02	1.82	+0.02	0.00	1.80
Mn1-O3	1.90	+0.03	−0.03	+0.04	1.89	+0.02	−0.04	+0.02	1.92	+0.05	−0.02	1.89	+0.02	+0.01	1.91	+0.04	+0.02	1.87
Mn1-O5	2.64	−0.06	−0.78	+0.49	2.51	−0.19	−0.66	+0.60	2.66	−0.04	−0.08	2.28	−0.42	+0.55	2.44	−0.26	+0.59	2.70
Mn2-O1	1.82	0.00	+0.00	−0.01	1.83	+0.01	−0.01	−0.01	2.12	+0.30	−0.30	1.83	+0.01	+0.01	1.78	−0.04	−0.01	1.82
Mn2-O2	1.77	−0.06	+0.01	+0.03	1.76	−0.07	0.00	+0.02	1.88	+0.05	−0.11	1.75	−0.08	+0.02	1.75	−0.08	+0.03	1.83
Mn2-O3	1.84	−0.18	+0.01	+0.02	1.83	−0.19	+0.01	+0.01	1.85	−0.17	0.00	1.84	−0.18	+0.01	1.85	−0.17	+0.02	2.02
Mn3-O2	1.84	−0.06	−0.02	−0.03	1.87	−0.03	−0.03	−0.04	1.85	−0.05	+0.02	1.92	+0.02	−0.05	1.82	−0.08	−0.03	1.90
Mn3-O3	1.98	−0.08	−0.03	−0.03	2.04	−0.02	−0.03	−0.01	1.98	−0.08	+0.05	2.08	+0.02	−0.06	1.97	−0.09	−0.03	2.06
Mn3-O4	1.83	−0.07	−0.02	+0.01	1.78	−0.12	−0.02	−0.01	1.85	−0.05	−0.02	1.78	−0.12	+0.09	1.83	−0.07	+0.02	1.90
Mn3-O5	1.76	−0.44	+0.11	+0.10	1.76	−0.44	+0.11	+0.07	3.13	+0.93	+0.03	2.32	+0.12	+0.01	1.75	−0.45	+0.07	2.20
Mn4-O4	1.80	−0.22	+0.01	−0.01	1.90	−0.12	+0.01	+0.02	1.81	−0.21	+0.03	2.02	0.00	−0.24	1.80	−0.22	−0.01	2.02
Mn4-O5	2.24	−0.09	+0.89	−0.42	2.29	−0.04	+0.82	−0.45	3.19	+0.86	+0.06	2.77	+0.44	−0.56	2.13	−0.20	−0.33	2.33
Ca-O1	2.44	−0.17	+0.05	+0.01	2.46	−0.15	+0.05	0.00	2.41	−0.20	+0.07	2.45	−0.16	0.00	–	–	–	2.61
Ca-O2	2.72	+0.05	+0.06	+0.09	2.74	+0.07	+0.04	+0.05	2.64	−0.03	+0.08	2.72	+0.05	+0.07	–	–	–	2.67
Ca-O5	2.53	−0.01	+0.09	+0.17	2.52	−0.02	+0.10	+0.14	2.50	−0.04	+0.04	2.43	−0.11	+0.02	–	–	–	2.54

Mn4-W1	2.26	+0.01	−0.12	−0.19	2.26	+0.01	−0.10	−0.18	2.17	−0.08	−0.03	2.21	−0.04	+0.03	2.33	+0.08	−0.21	2.25
Mn4-W2	2.04	−0.06	−0.02	−0.02	1.83	−0.27	−0.02	−0.02	1.93	−0.17	−0.02	2.22	+0.12	−0.16	2.02	−0.08	0.00	2.10
Ca-W3	2.46	−0.14	−0.03	−0.05	2.44	−0.16	−0.04	−0.04	2.49	−0.11	−0.04	2.50	−0.10	−0.02	–	–	–	2.60
Ca-W4	2.40	−0.07	−0.03	−0.03	2.42	−0.05	−0.03	−0.03	2.41	−0.06	−0.02	2.43	−0.04	−0.03	–	–	–	2.47
D170-Mn4	2.02	−0.01	−0.06	−0.04	2.05	+0.02	−0.05	−0.06	1.96	−0.07	+0.01	2.11	+0.08	−0.08	1.95	−0.08	−0.06	2.03
D170-Ca	2.53	+0.17	0.00	+0.01	2.50	+0.14	+0.02	0.00	2.42	+0.06	+0.02	2.53	+0.17	0.00	–	–	–	2.36
E189-Mn1	1.90	+0.11	−0.03	−0.04	1.93	+0.14	−0.03	−0.04	1.96	+0.17	−0.06	1.94	+0.15	−0.04	1.94	+0.15	−0.05	1.79
E189-Ca	2.77	−0.33	−0.14	−0.10	2.82	−0.28	−0.15	−0.09	3.10	0.00	−0.09	2.87	−0.23	−0.09	–	–	–	3.10
E333-Mn3	2.00	−0.06	−0.02	+0.01	1.99	−0.07	+0.08	+0.01	1.98	−0.08	−0.03	2.01	−0.05	−0.05	2.04	−0.02	0.00	2.06
E333-Mn4	1.98	−0.10	−0.06	−0.08	2.01	−0.07	−0.05	−0.09	1.97	−0.11	−0.02	2.18	+0.10	−0.16	2.12	+0.04	−0.13	2.08
D342-Mn1	2.19	−0.03	−0.05	−0.05	2.27	+0.05	−0.12	−0.14	2.19	−0.03	−0.03	2.32	+0.10	−0.15	2.36	+0.14	−0.19	2.22
D342-Mn2	2.08	−0.05	−0.04	−0.01	2.11	−0.02	−0.04	−0.01	2.10	−0.03	+0.01	2.13	0.00	−0.01	2.11	−0.02	0.00	2.13
E354-Mn2	2.00	−0.13	−0.03	+0.02	2.01	−0.12	−0.04	0.00	2.21	+0.08	−0.19	2.02	−0.11	−0.02	2.06	−0.07	0.00	2.13
E354-Mn3	2.17	+0.04	−0.05	−0.14	2.22	+0.09	−0.05	−0.14	2.19	+0.06	−0.05	2.29	+0.16	−0.06	2.17	+0.04	−0.11	2.13
A344-Mn2	1.91	+0.01	−0.04	−0.01	1.93	+0.03	−0.05	−0.02	1.97	+0.07	−0.04	1.94	+0.04	−0.02	1.91	+0.01	−0.02	1.90
A344-Ca	2.54	+0.11	−0.01	0.00	2.56	+0.13	−0.02	−0.01	2.49	+0.06	−0.06	2.53	+0.10	0.00	–	–	–	2.43
H332-Mn1	2.02	−0.10	+0.02	−0.03	2.03	−0.09	+0.02	−0.02	2.05	−0.07	−0.04	2.05	−0.07	−0.02	2.08	−0.04	−0.03	2.12
RMSD		0.12				0.13				0.25			0.15					

[a] Atomic distance (Å). [b] Difference from the experimental value. [c] Change in distance by formation of the S_2 state (oxidized Mn is indicated in parentheses). [d] Experimental value of the XFEL X-ray structure (5).

Table S2. Normal mode assignments of the symmetric COO^- stretching vibrations of model ***1***

S_1			S_2 (Mn1 oxidized)			S_2 (Mn4 oxidized)		
Frequency (cm^{-1}) [a]	Intensity (km/mol)	Assignment	Frequency (cm^{-1}) [a]	Intensity (km/mol)	Assignment	Frequency (cm^{-1}) [a]	Intensity (km/mol)	Assignment
1280	144	E189	1281	109	E189	1262	279	E189
1285	80	A344	1290	108	A344	1286	90	E333
1307	182	E189	1291	149	E333	1288	73	A344
1340	382	A344	1330	392	A344	1292	219	E189
1355	70	D170	1337	45	E189	1333	329	A344
1363	179	E354, D342	1348	120	D342, E333	1351	198	E333, D170
1366	77	D61,D342	1349	166	D342, E333	1357	374	D170
1368	198	D342, E354, D61, E189, A344	1356	113	D170	1363	39	E333, D170
1378	76	E354, A344	1358	250	E354	1366	157	D170, E333
1378	252	E189, E354	1366	147	E189	1367	154	D342, E189
1380	85	E189, E354, A344	1367	42	D61, E333	1373	176	E189, E354, D342
1389	195	E333	1370	413	D170, D61, E333	1374	151	D61, E189, D342, A344
1400	383	D170	1376	38	D170, A344, E333	1374	42	D61, E189, D342, A344, E354
1410	261	D61, D342	1377	99	E354, D170, A344	1377	163	E189, A344, D342, E354
1411	113	D342, D61	1378	211	D170, A344	1384	224	E354
1413	75	E189	1409	159	D342	1419	330	D61, D342
			1412	198	D61	1420	160	D342, D61
			1421	42	E189, E333	1448	158	E189
			1422	106	E333, E189			
			1439	107	E189			

[a] Calculated frequencies were scaled with a factor of 0.9593 to adjust the frequency of a major peak of the calculated S_2/S_1 difference spectrum (an average spectrum of Mn1- and Mn4-oxidized S_2) to 1401 cm^{-1}, where an intense negative band is located in the experimental spectrum.

Table S3. Normal mode assignments of the symmetrical COO^- stretching vibrations of model ***2***

S_1			S_2 (Mn1 oxidized)			S_2 (Mn4 oxidized)		
Frequency (cm^{-1}) [a]	Intensity (km/mol)	Assignment	Frequency (cm^{-1}) [a]	Intensity (km/mol)	Assignment	Frequency (cm^{-1}) [a]	Intensity (km/mol)	Assignment
1278	178	E189	1264	413	E189	1276	317	E189
1284	87	A344	1288	65	A344, E189	1288	77	A344
1305	212	E189	1290	189	A344, E189	1302	165	E189
1325	80	D170	1312	36	E333	1304	85	E333
1344	374	A344	1327	43	D170	1339	378	A344
1351	93	D170	1334	419	A344	1360	123	D170
1362	169	D342, E354, E189	1346	64	E189	1370	108	D342, E189
1364	74	D61	1351	53	D170	1371	113	D61
1367	168	E354, D342	1352	239	D342, E333, E354	1374	106	E354, E189
1376	72	E189	1354	61	E333, D342, E354, D170	1375	85	E189, E354
1376	121	E189, D342	1358	221	E354, A344, D342	1377	105	E189, D342
1379	89	A344, E354	1369	201	E189	1379	61	A344
1382	92	E354, A344, E189	1372	120	D61	1381	312	E333, D170
1395	248	E333	1379	83	A344, E354, E333	1386	302	D170, E333, E354
1400	45	A344	1383	171	E333	1389	133	E354, D170, E333, A344
1406	130	D342	1404	261	D170	1412	236	D61
1409	265	D170, D61	1408	152	D342	1421	237	D342
1410	96	D61, D342	1416	195	D61	1428	44	E333
			1422	54	E189			
			1433	46	E333, E354			

[a] Calculated frequencies were scaled with a factor of 0.9613 to adjust the frequency of a major peak of the calculated S_2/S_1 difference spectrum (an average spectrum of Mn1- and Mn4-oxidized S_2) to 1401 cm^{-1}, where an intense negative band is located in the experimental spectrum.

Table S4. Mulliken charges of the Mn and Ca ions calculated for high oxidation models

	model ***1***			model ***2***		
	Mulliken charge	ΔS_2 (Mn1)[a]	ΔS_2 (Mn4)[a]	Mulliken charge	ΔS_2 (Mn1)[a]	ΔS_2 (Mn4)[a]
Mn1	0.89	+0.24	+0.05	0.87	+0.26	+0.05
Mn2	1.10	+0.01	+0.00	1.09	+0.01	+0.00
Mn3	1.06	−0.06	−0.03	1.03	−0.07	−0.03
Mn4	0.90	+0.13	+0.20	0.85	+0.11	+0.20
Ca	1.12	+0.01	+0.02	1.11	+0.01	+0.02

[a] Change by formation of the S_2 state. Oxidized Mn is indicated in parentheses.

Table S5. OH bond lengths (Å) of water ligands (W3 and W4) of Ca^{2+}

	model ***1***			model ***2***		
water	S_1	ΔS_2 (Mn1)[a]	ΔS_2 (Mn4)[a]	S_1	ΔS_2 (Mn1)[a]	ΔS_2 (Mn4)[a]
W3	0.982	+0.001	+0.003	1.012	0.000	−0.002
	0.982	+0.005	+0.005	0.975	+0.003	+0.004
W4	0.982	+0.006	+0.005	0.980	+0.005	+0.004
	0.982	+0.002	+0.002	0.982	+0.002	+0.001

[a] Change by formation of the S_2 state. Oxidized Mn is indicated in parentheses.

SI Text: The Effects of Deprotonation of W2 on the Structure of the Mn_4CaO_5 Cluster and the COO^- Vibrations

The effects of deprotonation of W2 on the structure and ligand vibrations of the Mn_4CaO_5 cluster are revealed in the calculated data of models ***1*** and ***2***. The direct impact is shown at the shortened Mn4-W2 distance in model ***2*** by 0.21 Å (Table S1) due to a negative charge of OH^- and an increased basicity. This change in turn induces the changes in the positions of other ligands of Mn4. O5 and O4 are moved away from Mn4, resulting in increases in the Mn4-O5/O4 distances by 0.05/0.10 Å and decreases in the O5/O4-Mn1 distances by 0.13/0.05 Å. In addition, the Mn4-D170/E333 distances are increased by 0.07/0.03 Å. These changes further induce minor changes in some ligand distances of Mn3 and Mn1 (Mn3-O3, +0.06 Å; Mn3-E354, +0.05 Å; Mn1-E189, +0.03 Å; Mn1-D342, +0.08 Å), whereas little change is induced at Mn2 and Ca (≤ 0.03 Å except for +0.05 Å in Ca-E189). These structural changes are also reflected in the changes in the COO^- frequencies. In particular, direct carboxylate ligands of Mn4, D170 and E333, show slightly upshifted frequencies (Fig. S3; Tables S2 and S3). As a result, the symmetric COO^- vibration of D170 is coupled with the D61 vibration, which is originally located at a higher frequency in model ***1***. Other carboxylate vibrations also slightly change their frequencies and alter the couplings, resulting in the changes in the simulated band shapes. Nevertheless, the prominent feature of the calculated spectra in the COO^- region remains similar even upon W2 deprotonation, in contrast to the significant differences from the simulated spectra of the low-oxidation models (models ***3*** and ***4***; Fig. 2Ac, d).